Journal of Volcanology and Geothermal Research 259 (2013) 201–213

Contents lists available at SciVerse ScienceDirect

Journal of Volcanology and Geothermal Research

journal homepage: www.elsevier.com/locate/jvolgeores

Injection, transport, and deposition of tephra during event 5 at Redoubt Volcano, 23 March, 2009

Larry G. Mastin [a,*], Hans Schwaiger [b], David J. Schneider [b], Kristi L. Wallace [b], Janet Schaefer [c], Roger P. Denlinger [a]

[a] U.S. Geological Survey, 1300 SE Cardinal Court, Bldg. 10, Suite 100, Vancouver, WA 98683, USA
[b] U.S. Geological Survey, 4230 University Drive, Anchorage, AK 99508, USA
[c] Alaska Division of Geological and Geophysical Surveys, 3354 College Road, Fairbanks, AK 99709, USA

ARTICLE INFO

Article history:
Received 3 June 2011
Accepted 20 April 2012
Available online 5 May 2012

Keywords:
Tephra fall hazards
Tephra modeling
Alaska
Redoubt Volcano
Particle aggregation

ABSTRACT

Among the events of the 2009 eruption at Redoubt Volcano, Alaska, event 5 was the best documented by radar, satellite imagery, and deposit mapping. We use the new Eulerian tephra transport model Ash3d to simulate transport and deposition of event 5 tephra at distances up to 350 km. The eruption, which started at about 1230 UTC on 23 March, 2009, sent a plume from the vent elevation (estimated at 2.3 ± 0.1 km above sea level or a.s.l.) to about 16 ± 2 km above sea level in 5 min. The plume was a few kilometers higher than would be expected for the estimated average mass eruption rate and atmospheric conditions, possibly due to release of most of the eruptive mass in the first half of the 20-minute event. The eruption injected tephra into a wind field of high shear, with weak easterly winds below ~3 km elevation, strong southerly winds at 6–10 km and weak westerlies above ~16 km. Model simulations in this wind field predicted development of a northward-migrating inverted "v"-shaped cloud with a southwest-trending arm at a few kilometers elevation, which was not visible in IR satellite images due to cloud cover, and a southeast-trending arm at >10 km elevation that was clearly visible. Simulations also predicted a deposit distribution that strongly depended on plume height: a plume height below 15 km predicted ash deposits that were located west of those mapped, whereas good agreement was reached with a modeled plume height of 15–18 km. Field sampling of the deposit found it to contain abundant tephra aggregates, which accelerated the removal of tephra from the atmosphere. We were able to reasonably approximate the effect of aggregation on the deposit mass distribution by two methods: (1) adjusting the grain-size distribution, taking the erupted mass <= 0.063 mm in diameter and distributing it evenly into bins of coarser size; and (2) moving 80–90% of the mass <= 0.063 mm into a single particle bin ranging in size from 0.25 to 1 mm. These methods produced an area inside the 100 g m^{-2} isomass lines that was within a few tens of percent of mapped area; however they under-predicted deposit mass at very proximal (<50 km) and very distal (>250 km) locations. Modeled grain-size distributions at sample locations are also generally coarser than observed. The mismatch may result from a combination of limitations in field sampling, approximations inherent in the model, errors in the numerical wind field, and aggregation of particles larger than 0.063 mm.

Published by Elsevier B.V.

1. Introduction

The 2009 eruption of Redoubt Volcano was the most recent of several eruptions in recent decades to threaten communities around the northern Cook Inlet and Matanuska/Susitna region with tephra fall. Of the more than 19 explosive events in the 2009 eruption, event 5, which occurred at 1230–1250 Coordinated Universal Time (UTC) on 23 March 2009, was best documented from satellite observations, radar, and deposit sampling. In this paper we study the tephra dispersal from event 5 by comparing observations with numerical simulations. Such comparison allows us to examine the effect of plume height, particle-size distribution, and vertical distribution of mass in the plume, and narrow down the range of possible source-term values that controlled the final outcome. By examining the misfit between our best model results and observations, we can also examine the importance of processes that are not adequately modeled.

2. Observations

2.1. Plume development

Seismic records indicate that event 5 started at 1230 UTC on 23 March, 2009 (Buurman et al., 2013). Seismic shaking was energetic in the first few minutes, diminished slightly over the next several minutes,

* Corresponding author. Tel.: +1 360 993 8925; fax: +1 360 993 8980.
E-mail address: lgmastin@usgs.gov (L.G. Mastin).

0377-0273/$ – see front matter. Published by Elsevier B.V.
doi:10.1016/j.jvolgeores.2012.04.025

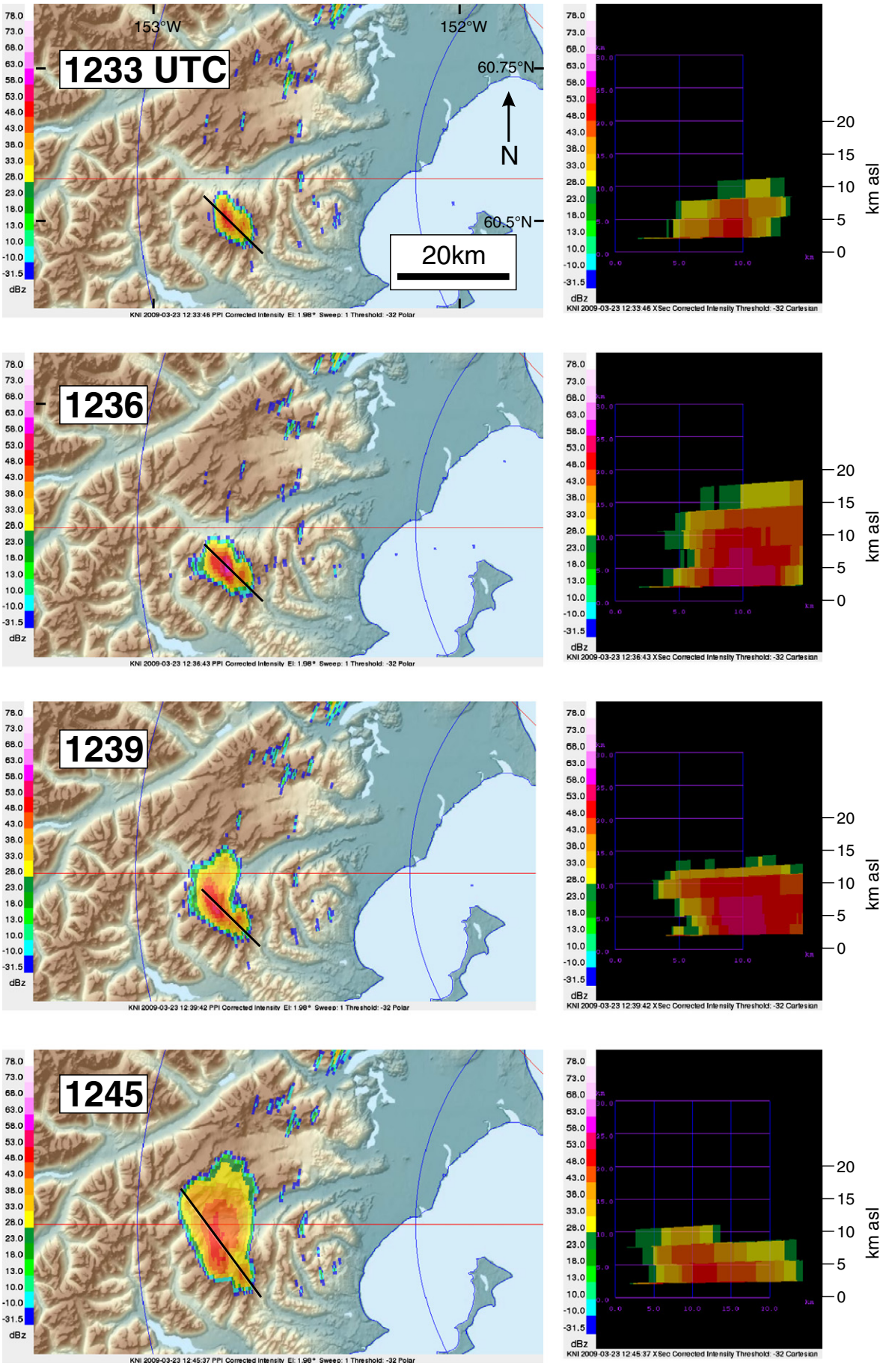
1233 UTC
153°W
152°W
60.75°N
60.5°N
N
20km
1236
1239
1245
dBz
km asl
0
5
10
15
20

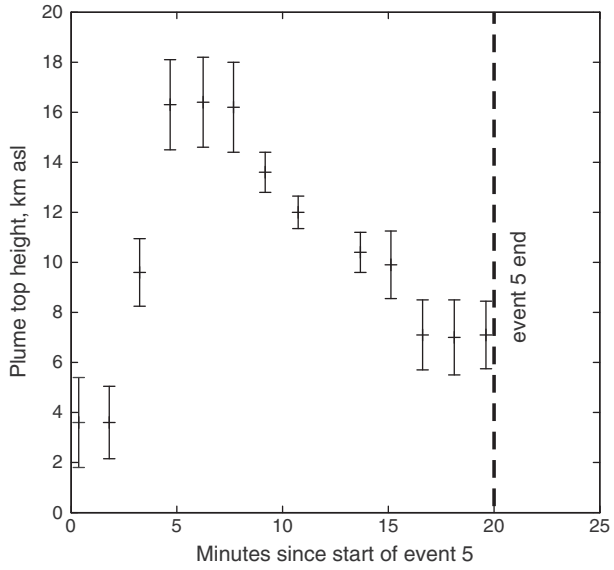

Fig. 2. Plot of plume height above sea level versus time in minutes since the start of event 5 at 12:30:30 UTC. Heights are taken from USGS Doppler radar data (Fig. 1). The error bars reflect the pixel height in the radar images shown in Fig. 1, which are related to the radar beam width at the distance of Redoubt Volcano from the radar system, located 82 km east of the volcano.

and then re-invigorated for about 5 min before gradually diminishing in the last 3–4 min of the 20-minute event (Buurman et al., 2013). The plume was clearly visible in retrievals from a 250 W U.S. Geological Survey radar system (Schneider and Hoblitt, 2013). Radar measurements (Figs. 1 & 2) show that the plume rose to 16 ± 2 km above sea level, or 14 ± 2 km above the vent, in about 5 min, an average ascent rate of about 30 m s^{-1}. It then dropped to about 12 km a.s.l. about 10 min after the eruption start, and gradually diminished until the eruption ended (Buurman et al., 2013) (Fig. 1).

Fig. 3 compares the plume height obtained from Doppler radar and ascent rate with values predicted by the one-dimensional steady plume model Plumeria (Mastin, 2007). Plumeria solves equations for mass, momentum, and energy to calculate the ascent velocity, plume radius, temperature, and the mass fraction of particles, air, and water in its various forms with elevation in the plume. Model inputs include a magma temperature of 900 °C, mass fraction gas of 3 wt.%, , exit velocity of 150 m s^{-1}, atmospheric temperature (Fig. 3b) and humidity obtained from a radiosonde launched from Anchorage at 1200 UTC on March 23. The dashed lines in Fig. 3c–e represent a plume having a mass eruption rate of 3.7×10^6 kg s^{-1}, estimated for event 5 using the mapped erupted mass (Wallace et al., 2013) and a 20-minute duration. The magma temperature and gas content are roughly consistent with Redoubt magmas (Swanson et al., 1994). The observed ascent time of ~5 min (Fig. 2) is greater than the ~3 min predicted for a plume of this eruption

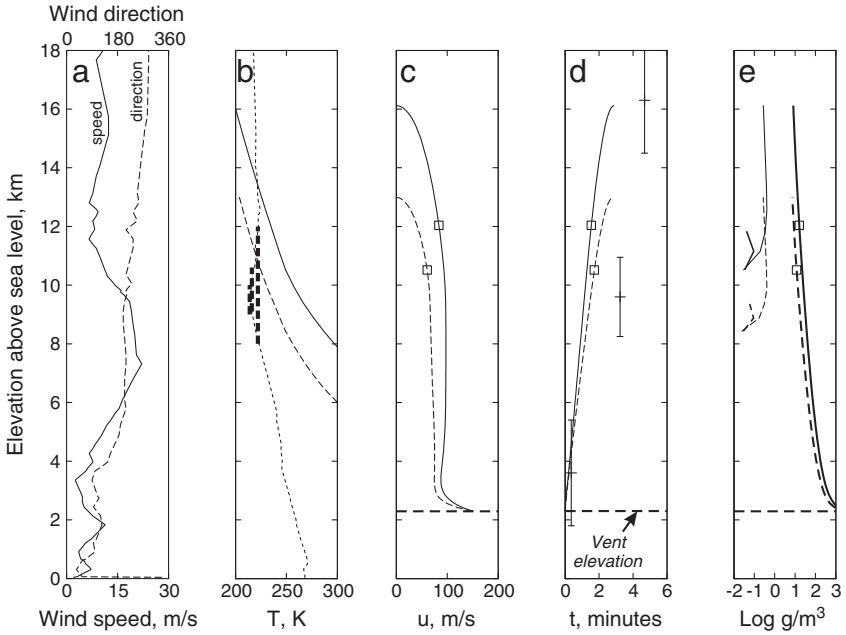

Fig. 3. Wind and plume properties as a function of elevation. (a) Wind speed (solid) and direction (dashed) measured by a radiosonde launched from Anchorage at 1200 UTC on 23 March, 2009. Wind direction is the direction from which wind is blowing in degrees east of true north. (b) Atmospheric temperature, from the same radiosonde (dotted), and temperatures of plumes modeled in Fig. 3c–e (solid and dashed). Three bold, vertical, dashed lines give the temperature of clouds in Fig. 4; the intersections of these lines with the temperature profile give the possible elevations of these clouds. (c) Upward velocity, (d) height versus time since start of plume, and (e) the log of the mass concentration of particles (bold lines), liquid water (medium lines), and ice (fine lines) in the plume, calculated by Plumeria (Mastin, 2007). Particle concentration decreases upward due to dilution with entrained air. The solid and dashed lines in (b–e) are for a plume having an exit velocity of 150 m s^{-1} and an initial magma temperature of 900 °C with 3 wt.% gas. The atmospheric temperature and humidity used in the model are those measured by the radiosonde. Dashed lines are for a plume having a mass eruption rate of 3.75×10^6 kg s^{-1} as estimated from maps of the event 5 deposit (Wallace et al., 2013) and the seismic duration; solid lines are for a plume having a mass eruption rate of 1.3×10^7 kg s^{-1}, which gives a plume height that agrees with the radar observations. The squares in (c–e) give the elevations of neutral buoyancy for the two model runs. The crosses with error bars in (d) give plume heights measured from radar.

Fig. 1. Corrected reflectivity plots of the event 5 ash cloud from the USGS radar system (Schneider and Hoblitt, 2013). On the left are reflective intensities (in dBZ) in map view from the lowest scan angle (1.98° degrees), illustrating the plume at about 3 km above sea level. On the right are cross sections of reflective intensity through the plume, at the locations of the black lines shown on the left plots. Elevation above sea level is shown on the axis on the right.

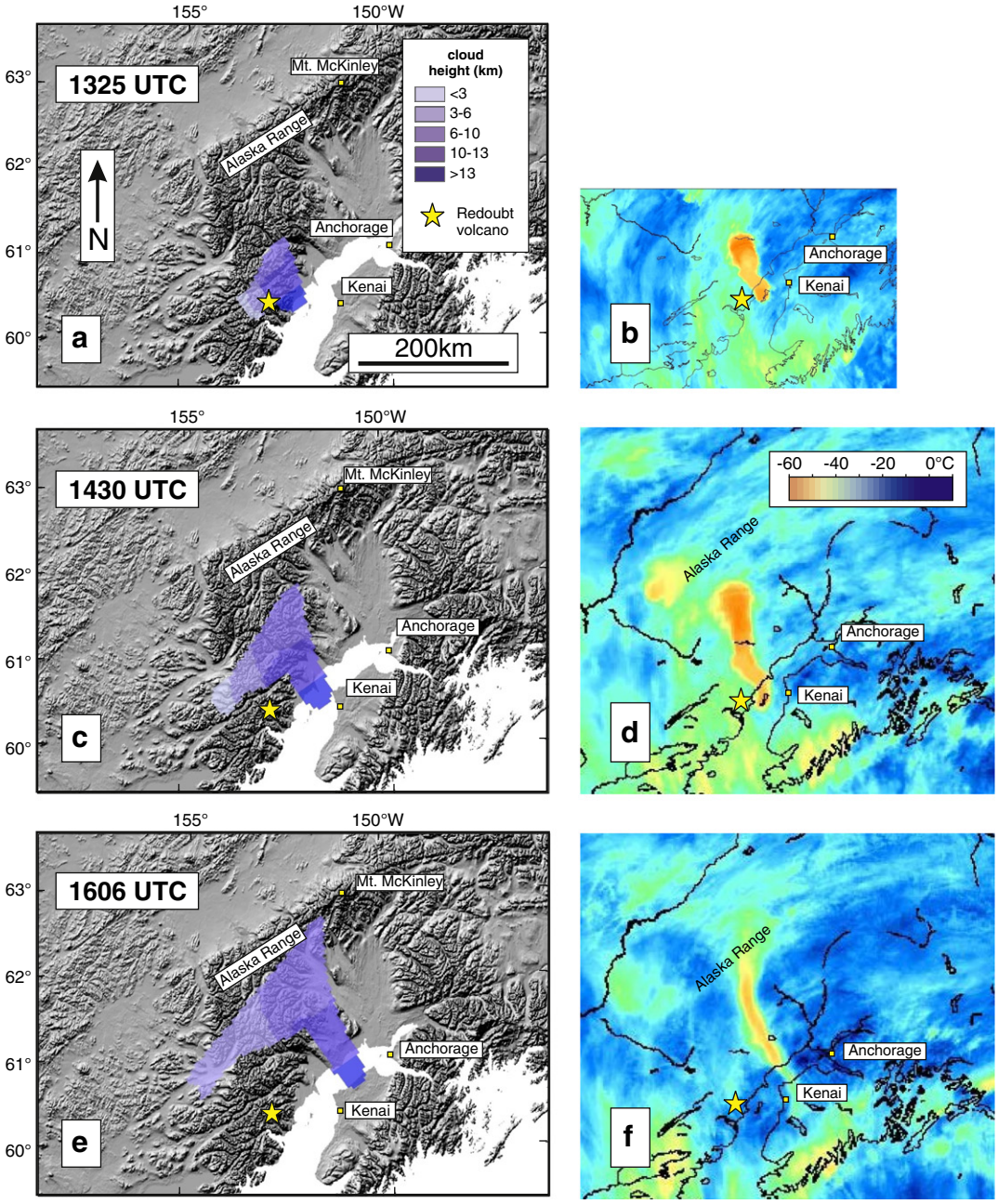

Fig. 4. Comparison of the event 5 ash cloud with satellite images. (a,c,e) Location and height of the event 5 ash cloud at 1325, 1430, and 1606 UTC as modeled using Ash3d for the input conditions given in Table 1 and grain-size distribution GSD0 (Table 3), assuming a 15-km-high plume. (b, d, f) Cloud temperature imaged by the AVHRR at the same times. The location of Redoubt Volcano is indicated with a yellow star. The deep yellow colors indicate cooler temperatures associated with the volcanic cloud. The cloud height in (a), (c), and (e) is shown only for portions of the cloud that exceed a load of 2 T km^{-2}, which is roughly the detection limit for ash clouds in some studies (Wen and Rose, 1994) that use the Brightness Temperature Difference method. AVHRR images were kindly provided by Peter Webley, University of Alaska, Fairbanks.

rate (Fig. 3d), a discrepancy that can largely be attributed to the fact that starter plumes like the observed one typically rise at about 60% the rate of a developed plume (Sparks et al., 1997, Section 5.4.1; Turner, 1962). More significantly, the observed height of 14 km above the vent was about 20% greater than that predicted by Plumeria (11.5 km) for a plume with the inferred eruption rate. It also exceeds heights of 10.6–11.6 km predicted by empirical height–eruption rate curves of Sparks et al. (1997, eq. 5.1) and Mastin et al. (2009, eq. 1) for this eruption rate. This discrepancy suggests a variable eruption rate wherein most of the mass may have erupted in the first half of the 20-minute event.

2.2. Ash cloud movement

Radar images (Fig. 1) show the event 5 cloud migrating northward almost immediately after injection into the atmosphere. These images show dBZ, a logarithmic portrayal of the cloud reflectivity which is a function of the number density and size of particles (Rinehart, 2004, Chapter 5). The northern boundary of the plume at a few kilometers elevation moved northward at a rate that decreased from about 45 m s^{-1} at 1236 UTC to 20 m s^{-1} at 1248 UTC. After 1248 UTC, the northern boundary began to stagnate, perhaps because coarse material was dropping out and reducing

Table 1
Input parameters used in the initial event 5 model run.

Parameter	Value
Start time	1230 UTC on 23 March, 2009
Duration, minutes	10
Erupted volume, m^3 DRE	1.7×10^6
Suzuki constant	8

Table 2
Total grain-size distribution estimated for the deposit by using the Voronoi tessellation technique (Bonadonna and Houghton, 2005) to combine the individual grain-size analyses of Wallace et al. (2013). The right column gives the time required for particles of each size to settle to sea-level elevation from a 15 km-high plume, using settling velocities of Wilson and Huang (1979) and integrating settling velocity with height, taking into account variations in air density and viscosity with elevation.

Size (mm)	Mass fraction	Hours to settle
31.5	0.0004	0.1
16	0.0083	0.1
8	0.0267	0.3
4	0.0306	0.4
2	0.0255	0.5
1	0.1082	0.8
0.5	0.1396	1.3
0.25	0.1120	2.7
0.125	0.1626	8
0.063	0.1154	30
0.031	0.1008	119
0.016	0.0767	476
0.008	0.0401	1905
0.004	0.0193	>2000
0.002	0.0115	>2000
0.001	0.0223	>2000

reflectivity below the −32 dbZ detection threshold. Infrared images from the Advanced Very High Resolution Radiometer (AVHRR) show the plume tracking to the north-northwest within an hour or so after the explosion start (Fig. 4; Webley et al., 2013). Minimum cloud temperatures in AVHRR images at 1325, 1430, and 1606 UTC are 214, 216, and 222 K in Fig. 4b, d, and f, respectively. Comparison with the radiosonde profile suggests that the minimum temperature at 1325 UTC corresponds to an elevation of about 9.4 km asl (Fig. 3b). The minimum temperature at 1430 UTC corresponds to an elevation of either 9.1 or 10.6 km, while that at 1606 UTC corresponds to either or 8.1 or 11.8 km asl. Schneider and Hoblitt (2013) argue convincingly that the cloud was stratospheric and the higher numbers are the correct ones.

Table 3
Grain-size distributions used in the model. The density values reflect the observation that the coarser particles consist primarily of pumice while the finer ones consist of glass, crystals, or some combination of the two.

Size (mm)	Mass fraction					Density ($kg\ m^{-3}$)
	GSD0	GSD1	GSD2	GSD3	GSD4	
16	0.0087	0.0521	0.0521	0.0087	0.0087	800
8	0.0267	0.0701	0.0701	0.0267	0.0267	800
4	0.0305	0.0740	0.0370	0.0305	0.0305	800
3	0	0	0.0370	0	0	800
2	0.0255	0.0689	0.0344	0.0255	0.0255	800
3	0	0	0.0344	0	0	800
1	0.1082	0.1516	0.0758	0.1082	0.4171	800
0.75	0	0	0.0758	0	0	800
0.5	0.1396	0.1831	0.0916	0.1396	0.1396	800
0.375	0	0	0.0916	0	0	1000
0.25	0.1120	0.1554	0.0777	0.5001	0.1120	1083
0.175	0	0	0.0777	0	0	1500
0.125	0.1626	0.2061	0.1031	0.1220	0.1626	1790
0.088	0	0	0.1031	0	0	2000
0.063	0.3861	0.0386	0.0129	0.0386	0.0772	2000
0.031	0	0	0.0129	0	0	2500
0.016	0	0	0.0129	0	0	2500

3. Modeling the event 5 ash cloud

In order to better understand the properties of the event 5 explosion, we modeled the ash cloud using a new tephra transport and dispersal model, Ash3d, developed by the U.S. Geological Survey (Schwaiger et al., 2012). It is a finite-volume Eulerian model that calculates tephra transport within a three-dimensional domain of cells and calculates the flux of tephra particles of all sizes through cell walls. The flux results from advective transport by wind, turbulent diffusion, and gravitational settling. Input values to Ash3d include a series of eruptive pulses which can be either contiguous or non-contiguous with time. Each pulse is specified with a plume height, erupted volume, start time, and duration. Also specified is a series of grain sizes with associated densities, and a Suzuki constant k (Suzuki, 1983) that determines the vertical mass distribution of tephra in the initial plume, following the equation (Suzuki, 1983; Carey, 1996)

$$\frac{dQ_m}{dz} = Q_m \frac{k^2(1-z/H)\exp(k(z/H-1))}{H[1-(1+k)\exp(-k)]}, \quad (1)$$

where Q_m is the total mass of erupted material in a given time step at a given particle size, H is the total plume height, and z is a given elevation in the plume. A low value of k gives a roughly uniform distribution of mass with elevation, while higher values concentrate mass near the plume top. Strong, vertical plumes concentrate ash in an umbrella cloud whereas weak bent plumes distribute ash over a wider range of elevations. The event 5 plume started out strongly but weakened with time. Our choice of $k=8$ is a compromise between these end members.

The model is initiated by distributing tephra in a column of cells immediately above the volcano. At each time step, the model calculates advective transport downwind using an explicit dimension-splitting method (LeVeque, 2002, Chapter 18). Turbulent diffusion is calculated implicitly, using a diffusion coefficient that is specified as input. Numerical diffusion causes some downwind widening of the cloud and the resulting deposit even when the diffusion coefficient is set to zero. After model predictions and observations from several other eruptions, we found that a non-zero value of the diffusion coefficient produced widening greater than observed, hence the diffusion constant was set to zero for our Redoubt event 5 runs.

The settling velocity of each pyroclast size is calculated at every elevation using the method of Wilson and Huang (1979), assuming a particle shape factor $f=0.44$, which was the average for pyroclasts measured by them ($f\equiv(b+c)/2a$, where a, b, and c are the semimajor, intermediate, and semiminor axes of an ellipsoid). We also apply a Cunningham slip-correction factor (Seinfeld and Pandis, 2006, p. 662), which modifies the no-slip condition on particle boundaries when the mean free path of an air molecule is significant relative to the particle's size. This factor substantially increases fall velocity for particles <0.03 mm at high altitude (Schwaiger et al., 2012). The transport of ash is calculated until the ash elevation equals the ground elevation. For topography, the model uses the GEBCO08 worldwide topographic dataset with 30 arc-second resolution,[1] corresponding to 930 m north–south and 450 m east–west at this latitude. Topographic features are smoothed using a rounding radius of 50 km to avoid isolated irregularities in deposit structure.

For the event 5 simulations, we used a three-dimensional wind field from the North American Regional Reanalysis (NARR) model.[2] The NARR files provide wind vectors at a horizontal nodal spacing of 32 km on a

[1] http://www.bodc.ac.uk/products/bodc_products/gebco/.
[2] http://dss.ucar.edu/pub/narr.

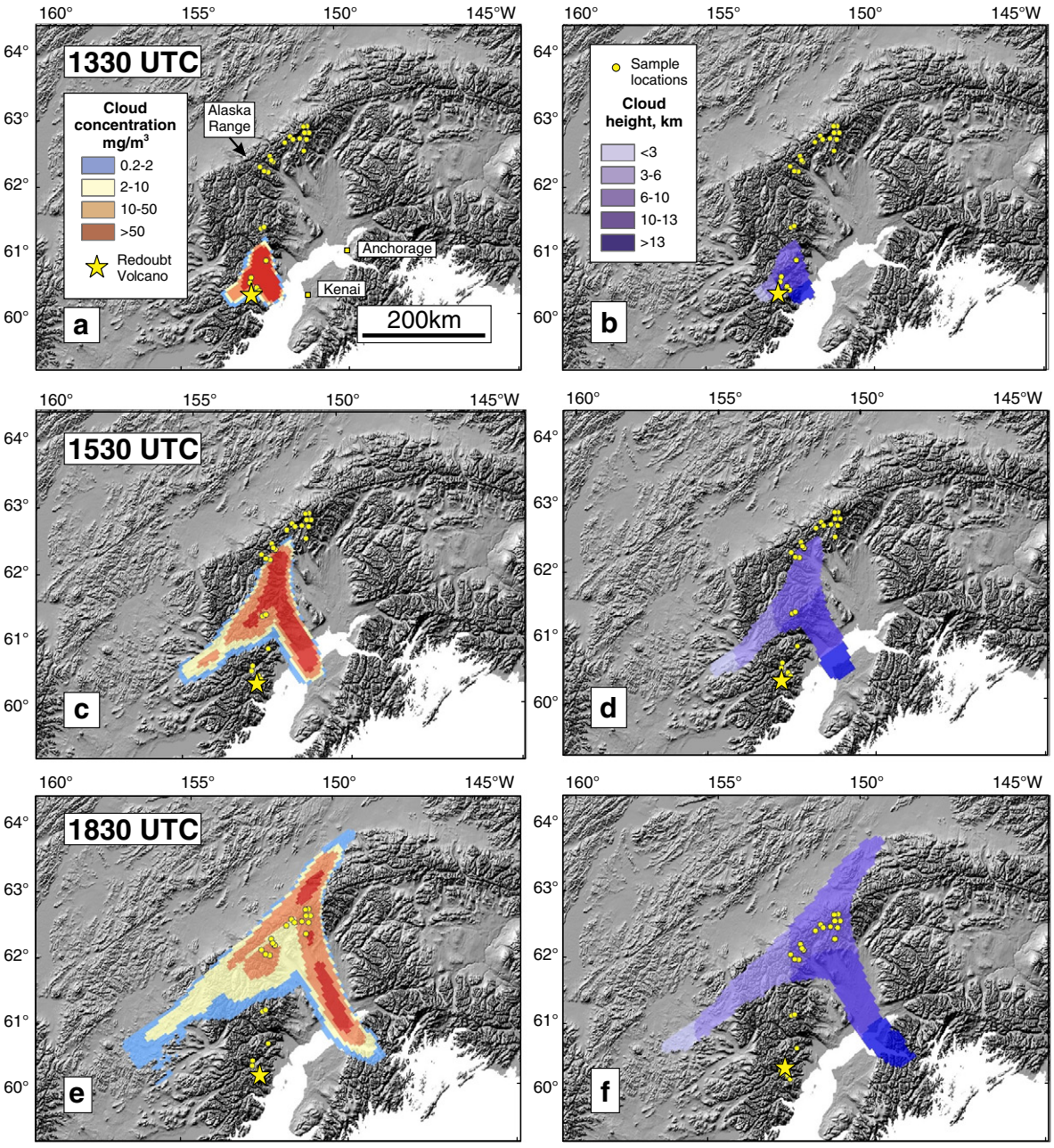

Fig. 5. Modeled ash cloud evolution. (a,c,e) Cloud concentration in mg m^{-3} of the event 5 cloud at 1330 (a), 1530 (c), and 1830 UTC (e) on 23 March, 2009, modeled for the input conditions in Table 1 using a 15-km-high plume and the grain-size distribution GSD0 in Table 3. The cloud concentration plotted represents the maximum concentration at any elevation in the column of nodes at that x, y location. (b,d,f) Cloud-top height from the same model run at 1330 (b), 1530 (d), and 1830 UTC (f), for portions of the cloud whose load exceeds 2 T km^{-2}.

Lambert conformal projection grid, with 29 pressure levels in the atmosphere from 1000 hPa (sea level) to 100 hPa (~16 km). NARR model results are updated every 3 h, and we interpolated linearly between these times to obtain wind vectors at each simulation time step (roughly once a minute). These values were then interpolated onto our model grid. We chose a horizontal spacing of 5 km and vertical cell spacing of 1 km, over a 700 × 700 km model domain centered at the volcano. This resolution was sufficient to replicate details like secondary thickness maxima while keeping simulation times less than 1 h. At elevations higher than 100 hPa (~16 km), we used the same wind vectors as in the topmost model node at a given location. Vertical wind velocity components were calculated by dividing vertical pressure velocities (in Pa s^{-1}) from the NARR model output by the average pressure gradient in the atmosphere at that elevation. The simulations were run for 20 h, which was enough time for most of the tephra to deposit or migrate out of the model domain.

3.1. Source parameters

In order to compare with observations, we executed a first model run using source parameters constrained from observations (Table 1). In particular, we used:

(1) A single eruptive pulse, an erupted mass of 1.7 million cubic meters dense-rock equivalent (DRE), and a duration of 10 min, roughly half the seismic duration, to reflect the fact that the

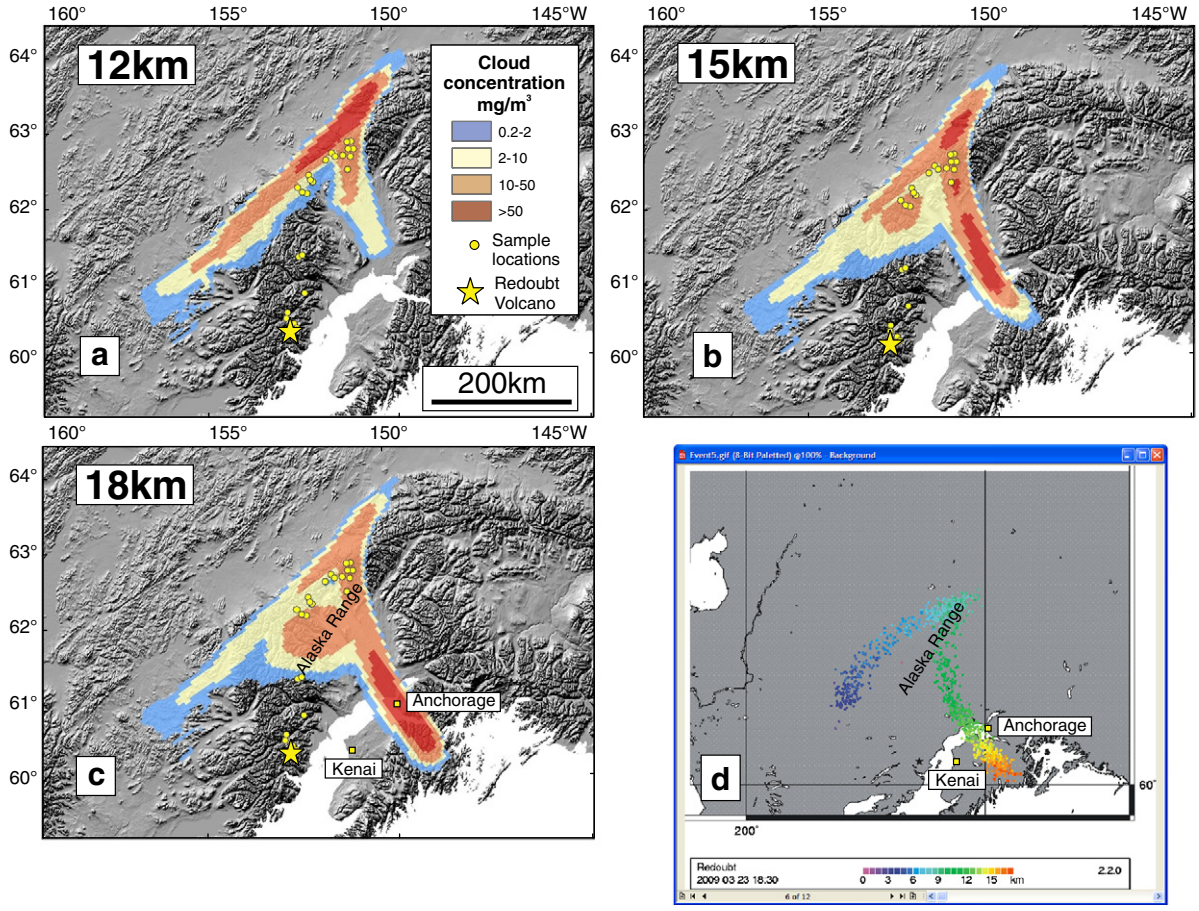

Fig. 6. Sensitivity of cloud shape to plume height and model type. Location and concentration (mg m^{-3}) of the modeled event 5 ash cloud at 1830 UTC assuming a plume top of 12 km (a), 15 km (b), and 18 km (c), and grain-size distribution GSD0 in Table 3. As in Fig. 5, the concentration plotted represents the maximum concentration within the column of nodes at a given x, y location. (d) Screenshot of the ash cloud forecast by the Puff model (Searcy et al., 1998) using a 16 km plume height. Particle colors in (d) give cloud height, with deep blue colors at about 3 km and red colors at about 16 km elevation.

most vigorous activity occurred during the first half of the 20-minute event. Plume heights in subsequent runs ranged from 12 to 18 km a.s.l.

(2) A Suzuki constant of 8, which concentrates about 90% of the erupted mass in the top half of the plume and distributes the remaining mass throughout the remaining column height.

(3) A total grain-size distribution that was simplified from results obtained by combining grain-size measurements of Wallace et al. (2013) using a Voronoi tessellation technique (Table 2). The result is a very rough representation of the total grain-size distribution because the sample locations are not distributed evenly throughout the deposit. About 62% of the deposit mass consists of particles larger than 0.063 mm in diameter. The mass and grain-size distribution of ash that was transported beyond the area mapped by Wallace et al. is unknown and was ignored in this study.

3.2. Accounting for particle aggregation

Like most tephra transport models, Ash3d does not consider aggregation of fine ash into clusters that fall out more rapidly than individual fine particles. This process was significant during event 5, as aggregates of ice and tephra were present at nearly all sample locations (Wallace et al., 2013). Using the method of Wilson and Huang (1979), we calculated the settling velocities of particles in Table 2, and integrated these velocities with distance along a falling trajectory to obtain the settling time from 15 km elevation (Table 2, column 3). By this calculation, particles 0.063 mm in diameter and smaller would not have settled over the 20-hour simulation time, even though they were shown to compose nearly 40% of the deposit mass. Therefore, to reduce the number of size bins and speed up model run time, we lumped all particles smaller than 0.125 mm into a single size bin of 0.063 mm diameter (Table 3, column 2, labeled "GSD0").

This modification did not account for particle aggregation however, since little of the ash in the finest bin would settle in 20 h if it fell at the settling rate calculated by the model. Previous modeling studies have accounted for particle aggregation through a variety of schemes. The simplest has involved setting a lower limit of 0.3–1.0 m s^{-1} to the settling velocity of fine ash. Carey and Sigurdsson (1982) used this approach when modeling the May 18, 1980 Mount St. Helens deposit, using a minimum velocity of 0.35 m s^{-1}, and were able to reproduce the secondary thickness maximum in Ritzville, Washington. Armienti et al. (1988), Macedonio et al. (1988), and Hurst and Turner (1999) have also used minimum settling velocities of 0.6–1 m s^{-1} for eruptions at Vesuvius, Mount St. Helens, and Ruapehu. Hopkins and Bridgman (1985) matched model results to the May 18, 1980 Mount St. Helens deposit by shifting the original grain-size distribution to produce a dominant mode at 0.063 mm and reducing the fraction at <0.010 mm. Cornell et al. (1983) matched the distribution of the Campanian Y-5

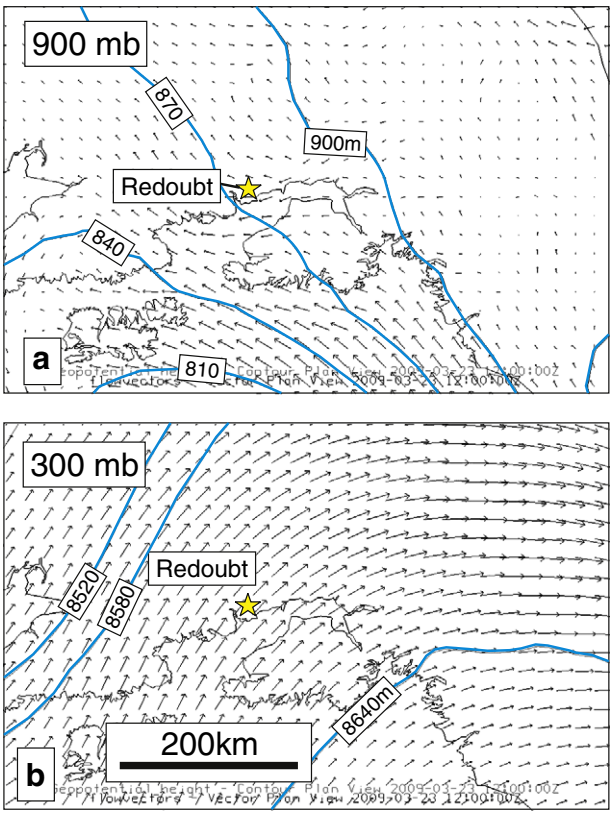

Fig. 7. Wind field in southern Alaska at the time of event 5. (a) Wind vectors at 900 mb (~800 m) elevation at 1200 UTC on 23 March 2009, taken from the North American Regional Reanalysis model. Blue bold lines are geopotential height in meters. (b) Wind vectors and geopotential height contours at 300 mb (~8.5 km) elevation. The Alaska coastline is shown in black thin lines. Wind vectors range from 0 to 50 m s^{-1}.

Ash by combining 50% of ash 0.125–0.063 mm in size, 75% of ash 0.063–0.031 mm, and 100% of ash <0.031 mm into aggregates 0.25 mm diameter having a density of 2000 kg m^{-3}. Bonadonna et al. (2002a) tested four different particle aggregation schemes when modeling fallout from dome-collapse events at Soufrière Hills volcano: the scheme of Cornell, and three schemes that aggregated 42–100% of ash <=0.063 mm into accretionary lapilli whose diameter was determined for each eruption from eq. (9) in Gilbert and Lane (1994). Folch et al. (2010) explicitly include a wet particle aggregation module in their Fall3d model and are able to reproduce the secondary thickness maxima of the May 18, 1980 Mount St. Helens and September 17–18, 1992 Mount Spurr deposits through inclusion of two parameters that describe particle aggregation efficiency and aggregate settling velocity.

To approximate the effects of particle aggregation, we tried a relatively simple adjustment in which 90% of the mass in the ≤0.063 mm GSD0 bin was distributed evenly among all the coarser bins, leaving only 10% of the original mass in the ≤0.063 mm bin (Table 3, column 3, labeled "GSD1"). This adjustment distributes the fine ash as a single mode throughout proximal and distal sections, consistent with observations of aggregation-dominated deposits (Brazier et al., 1983), and produces an ash cloud whose mass is a few percent of the total erupted mass, in agreement with ash cloud observations from other eruptions (Dacre et al. (in press); Wen and Rose, 1994). This adjustment assumes that most aggregation occurs quickly, within the rising plume rather than slowly in the ash cloud. That assumption is consistent with radar data (Schneider and Hoblitt, 2013) and deposit sampling, during which large ice aggregates were found even in the most proximal locations (Wallace et al., 2013).

The densities of particle aggregates may not coincide with that of pyroclasts of equal size, affecting their fall rate and depositional pattern. Densities have been estimated at 200–1300 kg m^{-3} for dry aggregates, 1200–1600 kg m^{-3} for accretionary lapilli, and 1000–1500 for mud rain (Sparks et al., 1997, Table 16.1); however densities of ice aggregates are not well characterized. Assuming that densities of ice aggregates are slightly (<10%) less than those of accretionary lapilli and mud rain due to the lower density of ice relative to water, the overall density range of these aggregates would still be within the range assigned to individual pyroclasts in Table 3, hence we see no justification for assigning separate bins with different densities for aggregates and pyroclasts.

For model runs using the GSD1 grain size, more than 98% of tephra was deposited within the 20-hour simulation time. Later in this paper we compare this modification with two others: (1) a scheme similar to that of Cornell et al. (1983); and (2) moving 80% of the 0.063 mm bin to the 1 mm bin.

3.3. Results

3.3.1. The ash cloud

Fig. 5 shows the modeled cloud concentration and cloud-top elevation predicted from Ash3d model simulations using the input parameters given in Table 1. The results at 1330 UTC show an ash cloud at the approximate location and elevation indicated by the AVHRR image (Fig. 4), with an incipient inverted "v" shape which becomes more apparent in subsequent images. The v-shape is apparent in all model runs for plume heights of 12–18 km (Fig. 6a–c), and in a run using the Puff Lagrangian volcanic ash transport and dispersion model (Searcy et al., 1998) for this event (Fig. 6d). This inverted "v" shape is not visible in satellite images (Fig. 4) because the lower, warmer leg of the cloud was obscured by meteorological clouds, and had a temperature close to ambient (Steensen et al., 2013).

The cloud's inverted "v" shape reflects complex winds caused by a low-pressure system centered in the Gulf of Alaska (Fig. 7). This low-pressure system produced weak westward-directed flow in the Cook Inlet area at low elevation (Fig. 7a) and strong north–northeast-directed winds at several kilometers elevation (Fig. 7b). Above about 14 km however winds were directed eastward (Fig. 3a). Thus low-level ash moved west, high-level ash moved east, and mid-level ash was carried north at the highest speed, forming the top of the inverted "v".

3.3.2. The tephra deposit

The complex wind pattern is also reflected in the distribution of tephra deposits. Fig. 8 illustrates the approximate extend of event 5 fallout mapped by Wallace et al. (2013) as yellow dots and orange lines, and those predicted by Ash3d as blue shading. The mapped isomass contours have values of 10 g m^{-2} (outer), 100 g m^{-2} (middle), and 1,000 g m^{-2} (inner). The 10 g m^{-2} isomass line was delineated from the edge of visible ash on the snow in MODIS images, which was found by sampling to have a mass loading of approximately 10 g m^{-2}. From Ash3d modeling, the isomass contour of 10 g m^{-2} is the outer boundary of the light blue shading; the 100 g m^{-2} contour is the outer boundary of the medium blue shading; and the 1,000 g m^{-2} contour is the boundary between the medium and dark blue shading.

From these images, two clear patterns emerge. First and most predictably, model runs using the grain-size distribution (GSD0) that doesn't consider particle aggregation (Fig. 8, left column) disperse tephra too widely, producing areas within the 10 g m^{-2} isomass that are too large, and those within the 100 g m^{-2} isomass, that are too small, when compared with the mapped distribution. The modified grain-size distribution (Fig. 8, right column) produces areas within the 10, 100, and 1000 g m^{-2} isomass lines that are closer to mapped values.

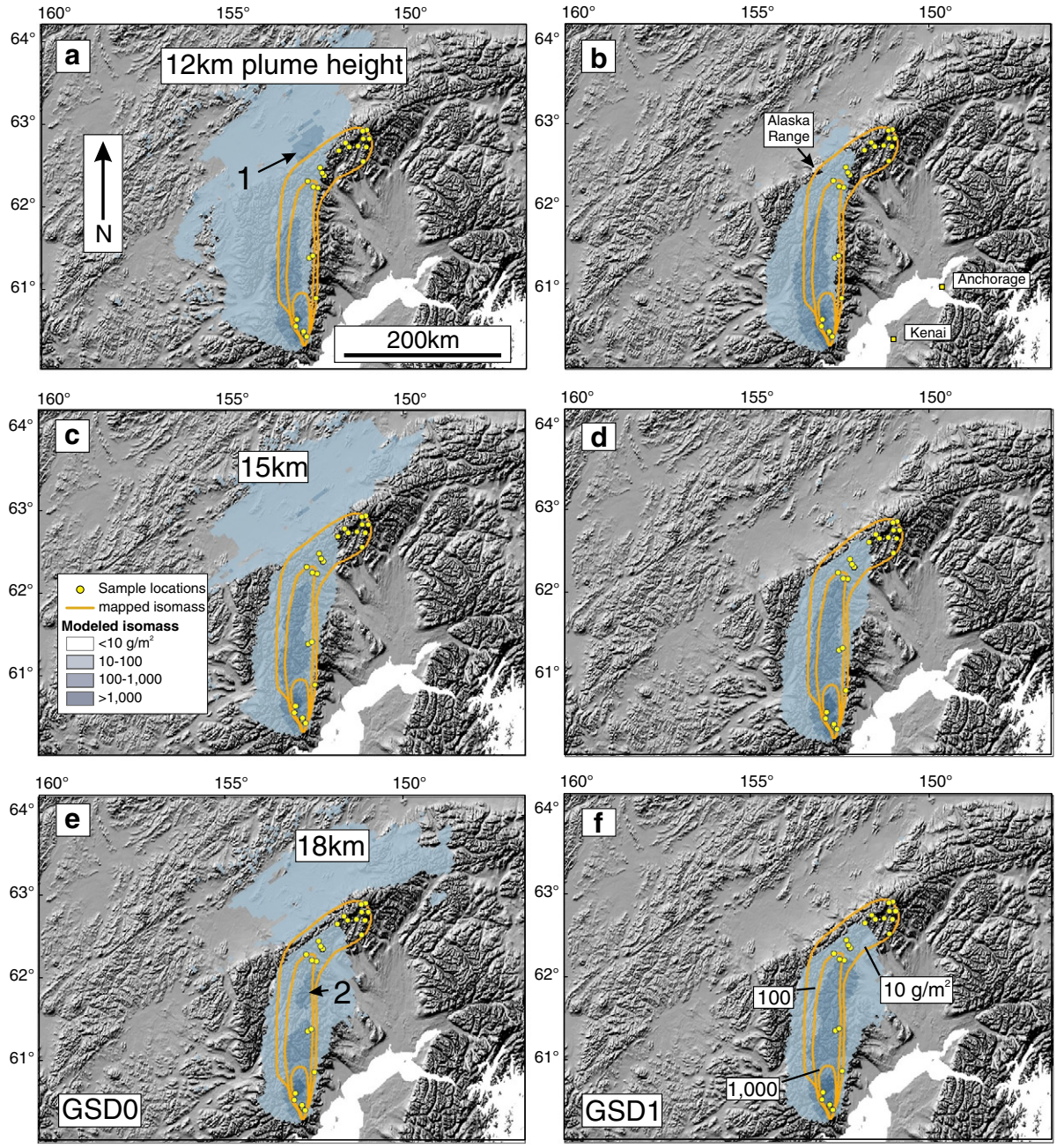

Fig. 8. Mass distribution of tephra from event 5 predicted by Ash3d model runs and measured by Wallace et al. (2013). The top, middle, and bottom rows represent model runs using a 12 km, 15 km, and 18 km plume height, respectively. The left and right columns represent model runs using grain-size distribution of GSD0 and GSD1, respectively (Table 3). Yellow dots are locations where tephra samples were collected and orange lines are hand-drawn contours of mass per unit area (Wallace et al., 2013). The outer orange line represents the outer boundary of ash on snow visible in MODIS images, which is estimated to represent a mass per unit area of about 10 g m^{-2} based on sampling. The central and inner orange contours are isomass lines of 100 and 1,000 g m^{-2} respectively. The light, medium, and dark blue shaded areas represent model predictions having mass loading of 10–100, 100–1000, and >1000 g m^{-2}, respectively.

Second, the low-level easterly winds shift the modeled deposit westward for runs in which a 12 plume height is used (top row). The 15- and 18-km-plume-height model runs locate the deposit, as judged for example by the 100 g m^{-2} isomass, closest to that mapped. On the other hand, the 12 km model runs seem to better replicate the overall deposit trend, moving north from Redoubt and then turning northeast when it meets the Alaska Range. None of the model simulations produced an isomass contour of 10 g m^{-2} that agrees especially well with the observed location.

These relationships are also apparent in the mass loadings measured and modeled at sample locations (Fig. 9). Model runs using a 12-km plume height and grain size GSD0 under-predict the mass loading at nearly all locations due to the neglect of particle aggregation and the westward displacement of the deposit by low-level winds. One site at about 125 km distance, for example, lies on the eastern edge of the deposit (Fig. 8) and under-predicts the deposit load by nearly three orders of magnitude. Both of these effects are reduced in the 15 km-GSD1 run and more so in 18 km-GSD1 run, resulting in a good fit with

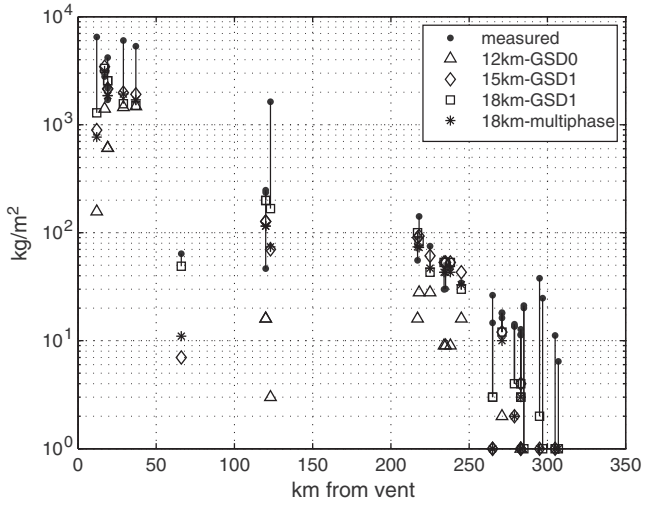

Fig. 9. Mass per unit area measured as a function of distance from the vent. Dots are values measured by Wallace et al. at sample locations. Triangles are values predicted by the model run using a 12 km plume height and the GSD0 grain-size distribution of Table 3. Diamonds are modeled values using a 15 km plume height and the GSD1 grain-size distribution. Squares are those predicted using an 18 km plume height and the GSD1 grain-size distribution. Stars are those predicted using the GSD1 grain-size distribution and an eruption consisting of four five-minute phases whose plume heights and volumes are given in Table 5. Vertical lines connect the measured points with those predicted from the 18 km, GSD1 run.

data at a distance of about 200–250 km. But even these runs underpredict deposit load somewhat at sites <50 km and >250 km from the source.

Mismatches in mass loading at proximal locations could reflect limitations in both field sampling and in the model. In the field at <50 km distance, samples were difficult to obtain and to distinguish from deposits of events 2–4 or 6, which occurred within hours of event 5. In the model, limitations included (1) nodal resolution in proximal settings where spatial variations in mass loading are high; (2) limitations in the numerical wind field to resolve local topographic effects around the volcano; (3) approximations in the grain-size distribution; (4) a vertical distribution of mass that places tephra too high in the column; or (5) temporal variations, such as a low plume late in the explosion that would deposit proximally but not be accounted for using the single plume height given as input.

We tested possibility (4) by running the model with Suzuki constant of $k=2$, which provides a nearly uniform distribution of tephra with elevation. The result (Fig. 10d) extends the deposit too far west and not far enough north to match observations. We also tested possibility (5) by dividing the explosion into four five-minute phases, each with its own plume height and eruption rate, as listed in Table 5. The result (Fig. 10c) places the proximal deposit west of the observations, and doesn't significantly reduce the discrepancy with proximal mass loading measurements in Fig. 9.

Fig. 11 compares measured grain-size distribution at four locations with those modeled using the 18 km, GSD1 model run (Fig. 8f). The measured grain-size distribution represents disaggregated particle size as measured in the laboratory rather than the actual size distribution of the deposited particles, which were primarily ice aggregates. Recall that the GSD1 grain-size distribution removed 90% of the mass in bins of size <=0.063 mm and divided it evenly among the coarser bins. For comparison in Fig. 11, we attempted to place the fine mass fraction back in the <=0.063 mm bin by the following method: the GSD1 size distribution increased the mass fraction of, for example, the 8 mm bin from 0.0267 to 0.0701. In constructing the 8 mm bin in Fig. 11 we multiplied its mass by 0.0267/0.0701, and moved the remaining mass back to the <=0.063 mm bin. The results show modeled particle sizes that are generally coarser than the disaggregated measured size, and a larger mass fraction of material in the <=0.063 mm bin. A possible explanation for the coarser size of the modeled deposit is that the density of aggregates was actually greater than that of equivalent-sized pyroclasts, causing them to settle out closer to the vent than predicted. After conducting more than two dozen model runs to test this hypothesis it became clear that the aggregate density does not affect the grain-size distribution of particles larger than 0.063 mm at a given location. A second possible explanation is that some particles coarser than 0.063 mm were aggregated, and that the aggregation of those particles was not considered in the grain-size adjustment used in the model. A third possibility is that a low plume late in the eruption deposited fine ash in proximal locations that could not have been deposited by the high, top-heavy plume we modeled. This last possibility would require that low-level winds at Redoubt be more southerly than given in the NARR model.

An intriguing feature in our modeled deposits is the occurrence of secondary thickness maxima, for example in Fig. 8a ("1") and e ("2"). The one in Fig. 8a is especially intriguing since it occurs near the elongated, northwest trending section of the mapped deposit at about 200–250 km distance. We hypothesize that the location, size, and perhaps existence of these secondary maxima are partially artifacts of the choice of grain-size bins. We tested this hypothesis by re-running the 12- and 18 km plume runs using a larger number of particle bins (GSD2, Table 3), in which we split some bins in two and divided the 0.063 mm bin into 0.063, 0.031, and 0.016 mm bins. The resulting deposits (Fig. 10a, b) show no secondary maxima, seeming to support our hypothesis. We tested two more grain-size distributions and found effects in both the area covered by ash and the location of the secondary maximum. In the first (GSD3, Table 3), we followed a procedure resembling that of Cornell et al. (1983): keeping in mind that our grain sizes represented the boundaries of grain-size ranges used by them, we moved 25% of the 0.125 mm particles and 90% of the <=0.063 mm particles to an aggregate of size 0.25 mm. In the second (GSD4, Table 3), we moved 80% of the particles <=0.063 mm into an aggregate 1 mm in diameter. Aggregate sizes noted in the field were mostly 0.5–2 mm (Wallace et al., 2013, Fig. 13). Both runs (Fig. 10e, f) predicted a secondary maximum within the mapped 100 g m^{-2} isomass line. No field samples were collected near these secondary maxima that could be used for validation. Both model runs also predict that the >100 g m^{-2} isomass region does not extend quite as far as mapped, and therefore they do not appear to match qualitatively with the mapped result as well as the GSD1 model run. The areas within the 100 g m^{-2} isomass for the GSD3 and GSD4 runs actually match the mapped area slightly better than that of GSD1 (Table 4). The importance of this comparison is difficult to assess, since the mapped 100 g m^{-2} isomass line is not well constrained by observations. The downwind extent is slightly better constrained with several samples at 200–250 km distance.

4. Discussion

In attempting to account for particle aggregation, we obtained our best qualitative fit by redistributing the finest (<=0.063 mm) fraction evenly among coarser bins. Schemes that redistribute the finest ash to a single coarser bin, 0.25 mm or 1 mm (GSD3 and GSD4) concentrate mass closer to the vent than observed, though the area they covered within the 100 g m^{-2} isomass line fits better with the mapped value than that the GSD1 run. One could envision a physical basis for different approaches depending on circumstances. Eruptions at Soufrière Hills Volcano were dome-collapse events whose size distribution was dominated by very fine (<0.063 mm) ash (Bonadonna et al., 2002b). They erupted into a warm, humid environment, where the dominant aqueous phase in the plume was liquid water, whose sticking efficiency

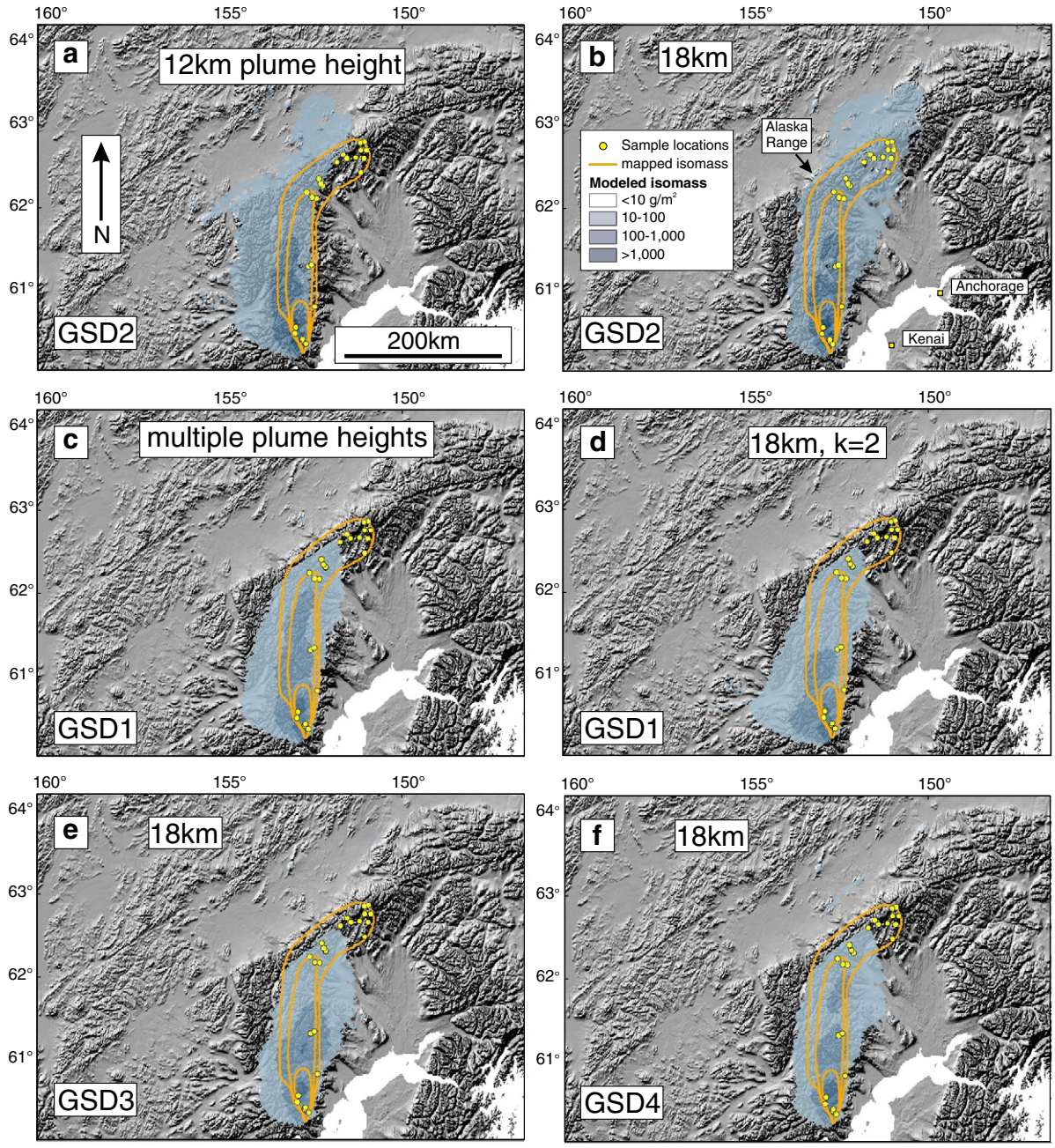

Fig. 10. Sensitivity of input parameters to deposit distribution. Plots show deposit distributions for (a) a 12-km plume height and grain-size distribution GSD2 in Table 3; (b) an 18-km plume height and grain-size distribution GSD2; (c) grain-size distribution GSD1 and an eruption that is divided into four five-minute phases whose eruption parameters are given in Table 5; (d) an 18-km plume height, grain-size distribution GSD1, and a Suzuki constant of $k=2$ (other runs use $k=8$); (e) an 18 km plume height with grain-size distribution GSD3; and (f) an 18 km plume height with grain-size distribution GSD4. The lines, symbols, and shading for the deposit are the same as for Fig. 8.

is several times greater than that of ice (Field et al., 2006). Those circumstances could promote rapid growth of a single aggregate size composed of fine particles. Redoubt event 5 tephra was coarser, ranged more widely in size, and erupted into a cold, ice-dominated plume, where small particles may have aggregated more slowly, by sticking to larger pre-existing particles.

Our simulated deposit distribution also agreed acceptably with observations when we used a plume height (15–18 km) and duration based on radar measurements. But we saw discrepancies that were difficult to reconcile, such as mismatches in mass loading in proximal and distal sites and a deposit that is either displaced westward in low-plume runs or doesn't hook to the northeast in high-plume runs. Attempts to reduce these discrepancies by varying grain-size distribution, vertical mass distribution in the plume, or adding a time-varying plume height, produced their own errors that were difficult to reconcile. The discrepancies are likely related to inherent approximations of the model, the coarse resolution of the wind field, limitations in field sampling on the ground, the fact that we had to accommodate aggregation through the crude method of redistributing grain sizes, and to our assumptions regarding aggregate density. The discrepancies may also reflect errors in the numerical wind field. A lower plume almost certainly existed later in the explosion, but the model run that simulated this evolving plume height (Fig. 10c) sent tephra too far west. These results

Table 4
Mapped and modeled areas within the 10, 100, and 1,000 g m^{-2} isomass lines.

Isomass area	Mapped km^2	Modeled, km^2			
		18 km GSD0	18 km GSD1	18 km GSD3	18 km GSD4
>10 g m^{-2}	14,980	48,800	24,030	22,450	22,750
>100 g m^{-2}	6270	5450	8480	7500	5600
$>1{,}000$ g m^{-2}	1170	430	980	530	900

Table 5
Eruption parameters for the phases used in model run illustrated in Fig. 10c. The explosion is divided into multiple phases whose plume height roughly equals that for each time interval in Fig. 2. The erupted volume for each phase was calculated using the empirical plume height–eruption rate relationship of Sparks et al. (1997, eq. 5.1). Using that relationship, the erupted volume summed to 2.48×10^6 m^3, which exceeded the 1.7×10^6 m^3 estimated erupted volume of Wallace et al. (2013). Therefore the volumes for each time interval were multiplied by (1.7/2.48) to ensure that their sum equaled 1.7×10^6 m^3.

Start time on 23 March, 2009	Duration minutes	Plume height, km a.s.l.	Volume, $\times10^6$ m DRE
1230 UTC	5	8	0.055
1235 UTC	5	16	1.27
1240 UTC	5	11	0.295
1245 UTC	5	7	0.051

illustrate the difficulty of simulating tephra transport in an environment with strong wind shear.

Notwithstanding the above considerations, this study demonstrates that the new Ash3d model can forecast deposit distributions that are in broad overall agreement with observations when used with appropriate source parameters. Discrepancies and mismatches are minor, but will be studied in an effort to improve model accuracy and better understand eruption physics.

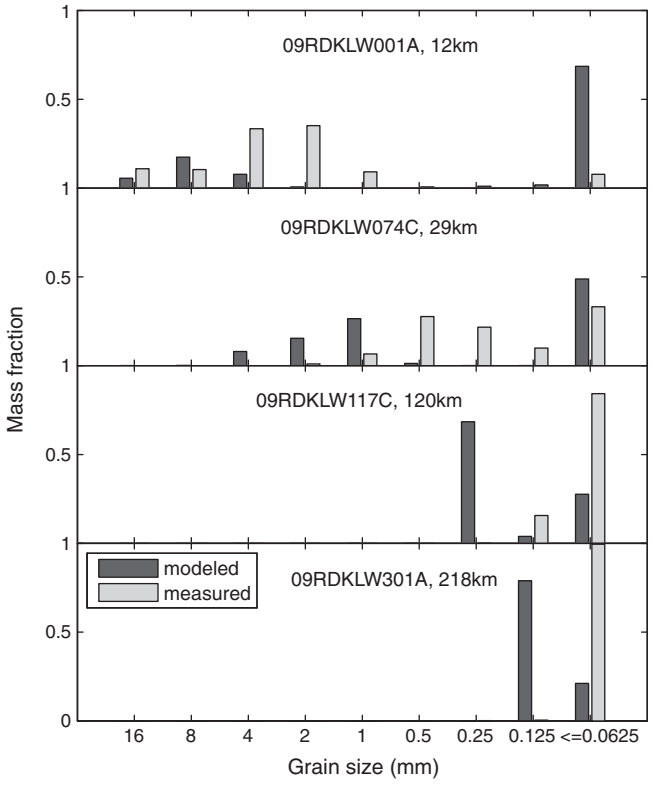

Fig. 11. Grain-size distributions measured (light gray) and modeled (dark gray) at four sampling locations. The sample name and distance of each location from the vent is given in the title to each plot. The model result illustrated in this figure used an 18 km plume and the GSD1 grain-size distribution. The grain-size adjustments used to derive this figure are described in the text.

Acknowledgments

We are grateful to many colleagues in the Alaska Volcano Observatory for the observations and logistical support for this study, in particular, Peter Webley, who kindly provided satellite infrared images of the event 5 cloud. We also acknowledge the helpful comments provided by three anonymous reviewers and by Guest Editor Chris Waythomas.

Appendix A. Supplementary data

Supplementary data to this article can be found online at http://dx.doi.org/10.1016/j.jvolgeores.2012.04.025.

References

Armienti, P., Macedonio, G., Pareschi, M.T., 1988. A numerical model for simulation of tephra transport and deposition: applications to May 18, 1980, Mount St. Helens eruption. Journal of Geophysical Research 93 (B6), 6463–6476.
Bonadonna, C., Houghton, B.F., 2005. Total grain-size distribution and volume of tephra-fall deposits. Bulletin of Volcanology 67, 441–456.
Bonadonna, C., Macedonio, G., Sparks, R.S.J., 2002a. Numerical modeling of tephra fallout associated with dome collapses and Vulcanian explosions: application to hazard assessment on Montserrat. In: Druitt, T.H., Kokelaar, B.P. (Eds.), the eruption of Soufriere Hills Volcano, Montserrat. Geological Society of London, London, pp. 517–537.
Bonadonna, C., Mayberry, G.C., Calder, E.S., Sparks, R.S.J., Choux, C., Jackson, A.M., Lejeune, A.M., Loughlin, S.C., Norton, G.E., Rose, W.I., Ryan, G., Young, S.R., 2002b. Tephra fallout in the eruption of Soufrière Hills Volcano, Montserrat. In: Druitt, T.H., Kokelaar, B.P. (Eds.), The eruption of Soufrière Hills Volcano, Montserrat, from 1995 to 1999. Geological Society of London, London, pp. 483–516.
Brazier, S., Sparks, R.S.J., Carey, S.N., Sigurdsson, H., Westgate, J.A., 1983. Bimodal grain size distribution and secondary thickening in air-fall ash layers. Nature 301, 115–119.
Buurman, H., West, M.E., Thompson, G., 2013. The seismicity of the 2009 Redoubt eruption. Journal of Volcanology and Geothermal Research 259, 16–30.
Carey, S., 1996. Modeling of tephra fallout from atmospheric eruptions. In: Scarpa, L.A., Tilling, R.I. (Eds.), Monitoring and Mitigation of Volcanic Hazards. Springer Verlag, Berlin, pp. 429–463.
Carey, S., Sigurdsson, H., 1982. Influence of particle aggregation on deposition of distal tephra from the May 18, 1980, eruption of Mount St. Helens volcano. Journal of Geophysical Research 87 (B8), 7061–7072.
Cornell, W., Carey, S., Sigurdsson, H., 1983. Computer simulation of transport and deposition of the campanian Y-5 ash. Journal of Volcanology and Geothermal Research 17 (1–4), 89–109.
Dacre, H.F., Grant, A.L.M., Hogan, R.J., Belcher, S.E., Thomson, D.J., Devenish, B., Marenco, F., Haywood, J., Ansmann, A., Mattis, I. (in press). The structure and magnitude of the ash plume during the initial phase of the Eyjafjallajökull eruption, evaluated using lidar observations and NAME simulations. Journal of Geophysical Research.
Field, P., Heymsfield, A., Bansemer, A., 2006. A test of ice self-collection kernel using aircraft data. Journal of the Atmospheric Sciences 63, 651–666.
Folch, A., Costa, A., Durant, A., Macedonio, G., 2010. A model for wet aggregation of ash particles in volcanic plumes and clouds: 2. Model application. Journal of Geophysical Research 115. http://dx.doi.org/10.1029/2009JB007176.
Gilbert, J.S., Lane, S.J., 1994. The origin of accretionary lapilli. Bulletin of Volcanology 56, 398–411.
Hopkins, A., Bridgman, C., 1985. A volcanic ash transport model and analysis of Mount St. Helens ashfall. Journal of Geophysical Research 90, 10620–10630.
Hurst, A.W., Turner, J.S., 1999. Performance of the program ASHFALL for forecasting ashfall during the 1995 and 1996 eruptions of Ruapehu volcano. New Zealand Journal of Geology and Geophysics 42, 615–622.
LeVeque, R.J., 2002. Finite Volume Methods for Hyperbolic Problems. Cambridge University Press, Cambridge. 553 pp.
Macedonio, G., Pareschi, M.T., Santacroce, R., 1988. A numerical simulation of the plinian fall phase of 79 A.D. eruption of Vesuvius. Journal of Geophysical Research 93 (B12), 14817–14827.
Mastin, L.G., 2007. A user-friendly one-dimensional model for wet volcanic plumes. Geochemistry, Geophysics, Geosystems 8 (Q03014). http://dx.doi.org/10.1029/2006GC001455.
Mastin, L.G., Guffanti, M., Servranckx, R., Webley, P., Barsotti, S., Dean, K., Denlinger, R., Durant, A., Ewert, J.W., Neri, A., Rose, W.I., Schneider, D., Siebert, L., Stunder, B., Swanson, G., Tupper, A., Volentik, A., Waythomas, C.F., 2009. A multidisciplinary effort to assign realistic source parameters to models of volcanic ash-cloud transport and dispersion during eruptions. Journal of Volcanology and Geothermal Research 186, 10–21.

Rinehart, R.E., 2004. Radar for Meteorologists. Rinehart Publications, Columbia, MO. 482 pp.
Schneider, D.J., Hoblitt, R.P., 2013. Doppler weather radar observations of the 2009 eruption of Redoubt Volcano, Alaska. Journal of Volcanology and Geothermal Research 259, 133–144.
Schwaiger, H.F., Denlinger, R.P., Mastin, L.G., 2012. Ash3d: A finite-volume, conservative numerical model for ash transport and tephra deposition. J. Geophys. Res. 117 (B4), B04204.
Searcy, C., Dean, K., Stringer, W., 1998. PUFF: a high-resolution volcanic ash tracking model. Journal of Volcanology and Geothermal Research 80, 1–16.
Seinfeld, J.H., Pandis, S.N., 2006. Atmospheric Chemistry and Physics: From Air Pollution to Climate Change. John Wiley & Sons, Hoboken, New Jersey. 1203 pp.
Sparks, R.S.J., Bursik, M.I., Carey, S.N., Gilbert, J.S., Glaze, L.S., Sigurdsson, H., Woods, A.W., 1997. Volcanic Plumes. John Wiley & Sons, Chichester. 574 pp.
Steensen, T., Stuefer, M., Webley, P., Grell, G., Freitas, S., 2013. Qualitative comparison of Mount Redoubt 2009 volcanic clouds using the PUFF and WRF-Chem dispersion models and satellite remote sensing data. Journal of Volcanology and Geothermal Research 259, 235–247.
Suzuki, T., 1983. A Theoretical Model for Dispersion of Tephra. In: Shimozuru, D., Yokoyama, I. (Eds.), Arc Volcanism: Physics and Tectonics. Terra Scientific Publishing Company, Tokyo, pp. 95–113.
Swanson, S.E., Nye, C.J., Miller, T.P., Avery, V.F., 1994. Geochemistry of the 1989–1990 eruption of Redoubt Volcano: Part II. Evidence from mineral and glass chemistry. Journal of Volcanology and Geothermal Research 62 (1–4), 453–468.
Turner, J.S., 1962. The starting plume in neutral surroundings. Journal of Fluid Mechanics 13, 356–368.
Wallace, K.L., Schaefer, J.R., Coombs, M.L., 2013. Character, mass, distribution, and origin of tephra-fall deposits from the 2009 eruption of Redoubt Volcano, Alaska—Highlighting the significance of particle aggregation. Journal of Volcanology and Geothermal Research 259, 145–169.
Webley, P.W., Lopez, T.M., Ekstrand, A.L., Dean, K.G., Rinkleff, P., Dehn, J., Cahill, C.F., Wessels, R.L., Bailey, J.E., Izbekov, P., Worden, A., 2013. Remote observations of eruptive clouds and surface thermal activity during the 2009 eruption of Redoubt volcano. Journal of Volcanology and Geothermal Research 259, 185–200.
Wen, S., Rose, W.I., 1994. Retrieval of sizes and total masses of particles in volcanic clouds using AVHRR bands 4 and 5. Journal of Geophysical Research 99 (D3), 5421–5431.
Wilson, L., Huang, T.C., 1979. The influence of shape on the atmospheric settling velocity of volcanic ash particles. Earth and Planetary Science Letters 44, 311–324.